

# White light generated by femtosecond optical vortex beams

P. HANSINGER<sup>1</sup>, G. MALESHKOV<sup>2</sup>, I. L. GARANOVICH<sup>3</sup>, D. V. SKRYABIN<sup>4,5</sup>, D. N. NESHEV<sup>3</sup>, A. DREISCHUH<sup>2,\*</sup>, AND G. G. PAULUS<sup>1,6</sup>

<sup>1</sup>Institute for Optics and Quantum Electronics, Friedrich-Schiller-University, Max-Wien-Platz 1, D-07743 Jena, Germany

<sup>2</sup>Department of Quantum Electronics, Sofia University, 5, J. Bourchier Blvd., Sofia-1164, Bulgaria

<sup>3</sup>Nonlinear Physics Centre, Australian National University, Canberra, Australia

<sup>4</sup>Department of Physics, University of Bath, Bath, BA2 7AY, United Kingdom

<sup>5</sup>ITMO University 197101, Kronverksky Avenue 49, St. Petersburg, Russian Federation

<sup>6</sup>Helmholtz Institute Jena, Helmholtzweg 4, D-07743 Jena, Germany

\*Corresponding author: ald@phys.uni-sofia.bg

Compiled January 24, 2016

In this work we report detailed experimental and numerical investigation of the white light generation by singly- and doubly-charged optical vortices propagating in a Kerr medium, where spectral broadening and transfer of topological charge (TC) into emerging spectral satellites takes place due to self-phase modulation and degenerate four-wave frequency mixing (FWM). Experiments performed with different pump beams show an excellent agreement with theory. Singly- and doubly-charged white light vortices are observed within more than  $\pm 200\text{nm}$  bandwidth after nonlinear propagation in Argon gas. Our experiment and theory data confirm that the topological charge transformation of the newly-generated spectral components follow a law analogous to the one for the energy conservation in the FWM process. We also present results on the white light vortex stability. © 2016 Optical Society of America

**OCIS codes:** (190.0190) Nonlinear optics; (190.4380) Nonlinear optics, four-wave mixing; (260.6042) Singular optics.

<http://dx.doi.org/10.1364/ao.XX.XXXXXX>

## 1. INTRODUCTION

Optical vortices (OVs) are singular beams with spiral phase dislocations in the wavefront [1]. The field at the singularity point (vortex core) has no defined phase and therefore the intensity must vanish, leading to a characteristic toroidal beam profile [2, 3]. OVs carry photon orbital angular momentum, which is independent of the photon spin and can be transferred to matter [4]. The angular momentum is proportional to the vortex topological charge (TC)  $l$ , which corresponds to the total phase change  $2\pi l$  over the azimuthal coordinate  $\varphi$ . Vortices are ubiquitous in nature and have become a research topic in many areas of physics, ranging from fluid dynamics [5] to cold atoms [6]. OVs have found useful applications in optical manipulation of small particles [7], in optical imaging [8], as potential information carriers in data transmission [9], in interferometry [10], high-resolution microscopy and lithography [11], in spectroscopy [12, 13] and in other areas.

Supercontinuum (SC) generation by ultra-short laser pulses is one of the fascinating nonlinear phenomena in optics [14]. SC finds many applications in frequency metrology [15], spectroscopy [16, 17], light sources development [18–20], and opti-

cal coherence tomography [21, 22]. First discovered in the early 70's in bulk glasses [23], SC generation from singular optical beams containing complex spatial and phase structure in self-focusing Kerr nonlinear media has remained unexplored for a long time. First experimental studies of SC generation with OVs were performed only recently [24, 25]. The SC generation process in  $\text{CaF}_2$  was determined mainly by the filamentation of the vortex ring. Strong diffraction of the SC generated by these filaments was the reason for the observed broad white-light background. The continua generated from the different filaments were, however, not coherently added into the output SC beam and the vortex phase profile was not transferred to all the newly generated frequency components.

Recently we reported on the first [26] successful experimental studies of the generation of SC light by OVs. Here we present a detailed experimental and numerical analysis of the vortex generation process, including its stability. In two different experimental setups we use short femtosecond pump pulses with embedded singly- and doubly-charged vortex beams. We focus them into an Argon-filled gas cell where relatively weak self-focusing and four-wave mixing in the thin cell input window and subsequent nonlinear interaction in the

gas induce spectral broadening and generate SC. Extensive numerical simulations confirm the physical mechanisms of the processes involved. New results here in addition to these in [26] are:

- i) The single-beam pumping experiment serving as a proof for the main findings obtained with the two-beam pumping scheme;
- ii) The detailed experimental study of the vortex stability vs. gas pressure;
- iii) The theoretical estimation of the saturation intensity and of the  $B$ -integral (i.e. the nonlinear contribution to the medium nonlinearity) vs. gas pressure;
- iv) The simulation of the output spectrum based on the developed continuous-wave model for the four-wave mixing and on an experimentally recorded input pump spectrum.

## 2. RESULTS

### A. Single-beam pumping with singly-charged OV

In the first experiment we placed one or two vortex lenses directly in the output beam of a 25-fs Ti:Sapphire amplified laser system delivering 1.25mJ pulses at 4kHz repetition rate (see Fig. 1). Both vortex lenses are commercially-available antireflection-coated 16-level spiral phase plates fabricated from fused silica. The (Ar-filled) gas cell was composed by 3 segments of total length of 213cm, with a 3mm thick Brewster-angle input and a perpendicular 1mm thick output fused silica window. The incoming beam was gently focused through the input window in the middle of the gas cell by a 2" silver-coated focusing mirror FM1 ( $f = 200cm$ ; see Fig. 1), and was refocused by a curved mirror FM2 with the same parameters. This configuration allows to use moderate nonlinearity inside the solid state material and to precisely control the nonlinear interaction near the focus (in the filament region) in the cell by controlling the gas pressure. Neutral density filters NDF are used to avoid saturation of the charge-coupled device camera CCD monitoring the interference patterns at the exit of the diagnostic Mach-Zehnder interferometer. One of the interferometer mirrors was mounted on a translation stage in order to be able to precisely overlap the interfering pulses in time. Bandpass filters with central transmission wavelength spaced at 50nm and with transmission bandwidths of 40nm were placed directly in front of the CCD camera in order to record interference patterns in the desired spectral regions only.

Our working hypothesis was that controllable SC generation by femtosecond optical vortex beams can be achieved by precise control of the four-wave frequency mixing (FWM) processes involved. When two pump beams at frequencies  $\omega_1$  and  $\omega_2$  interact in a Kerr-type nonlinear medium, the FWM process results in the generation of new distinct sum and difference frequency components  $\omega_s = 2\omega_i \pm \omega_j$  at the output. Importantly, unlike OV propagation in a Raman [27] or quadratic nonlinear medium [28] the FWM process is expected to preserve the topological charge of the OVs [29, 30] (in the last article - in first cascaded order of the FWM only). Thus, FWM can be employed for the generation of white-light vortices. In order to experimentally realize two (broadband) pump components at distinct frequencies, we split the spectrum of the femtosecond oscillator by programming the acousto-optical modulator (Fastlite DAZZLER) of the laser system accordingly. (In the time domain this causes oscillations in the wings of the pump pulse but we did not observe any negative effects from this.) In Fig. 2 we show the spectrum of the shaped pump pulses at

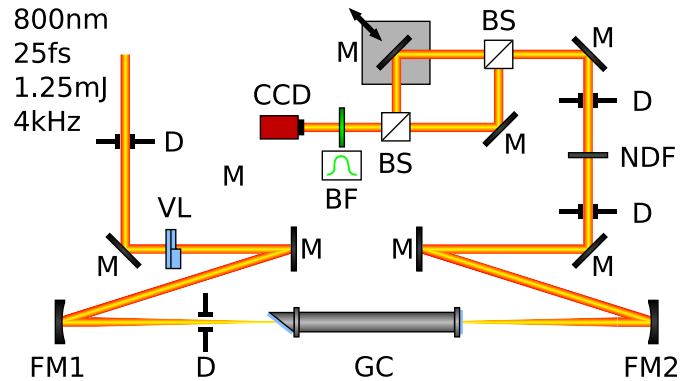


**Fig. 1.** (Color online) Experimental setup for generating white light vortices starting with OVs in a spectrum split with an acousto-optical modulator (DAZZLER). Diagnostics is done with a replica of the supercontinuum OV beam. M – protected silver-coated mirrors; D – iris diaphragm; VL – vortex lens (16-level spiral phase plate; fused silica); BF – bandpass filter ( $\lambda_C \pm 20nm$ ),  $\lambda_C$  – central wavelength; BS – beam-splitter; FM1 – 2" focusing mirror ( $f = 2m$ ); FM2 – 2" (re)focusing mirror ( $f = 2m$ ); NDF – neutral density filters; CCD – charge-coupled device camera (CMOS color camera Thorlabs Model DCC1645C or B/W CCD camera Pike F505B, Allied Vision Tech.). GC – Ar-filled gas cell 213cm long.

the input (black curve/open circles) and at the output of the gas cell (red/solid curve) for 0.5 – mJ / 25 – fs pulses (prior to pulse shaping) and at Ar-pressure of 1.3bar. As seen, the two pump wavelengths are centered at 770nm and 805nm. Therefore, the first side-lying peaks in the output spectrum centered at 748nm and 850nm correspond to first cascaded order FWM signals, and the left peak near 709nm (and the broad hump near 875nm) should come from second cascaded order FWM.

The key experimental data obtained with this setup are summarized in Figs. 3 and 4. We conducted interferometric measurements in every accessible 40 – nm-wide spectral window from 500nm to 850nm and for all spectral components with wavelengths exceeding 900nm. The results in the interval 850nm – 900nm are expected to be nearly the same but were not recorded because of the lack of a suitable bandpass filter. The typical measurements of interference of the output beam with itself are shown in Fig. 3. The characteristic fork-like splitting of one interference line into two lines indicates the location of the OV spiral phase dislocation (encircled in each frame of Fig. 3). It is interesting to note and it is intuitively clear that if the vortices are offset strictly along the interference lines, no line splits. This is because the two helical phase fronts influence the interference much like plane wavefronts do. If the OV offset is perpendicular with respect to the interference lines, the self-interference looks seemingly like two vortices of opposite TCs are present. The measurements with singly-charged pump OVs confirm that all spectral components in the generated continuum indeed carry single-charged OVs, leading to the nonlinear generation of white-light vortex beams.

By blocking one of the beams in the Mach-Zehnder interferometer we were also able to monitor the beam structure of the newly generated components in each spectral interval. As expected, near the pump components (e.g. at  $(750 \pm 20)nm$ ; see left frame in Fig. 4) the vortex ring remains still well preserved. The white light in the further-lying spectral components (e.g. at

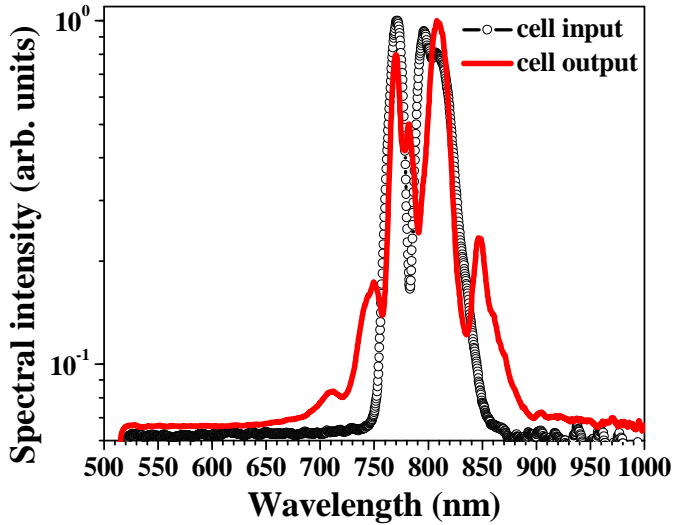


**Fig. 2.** (Color online) Spectrum of the pump pulses, shaped with an acousto-optical modulator (DAZZLER), at the input (black curve/open circles) and at the output of the gas cell (red/solid curve). Ar-pressure - 1.3bar. Pump pulses - 0.5mJ/4kHz/25fs (prior pulse shaping).

( $650 \pm 20$ )nm; see right frame in Fig. 4) shows a clear signature of three (diffracting) filaments.

### B. Single-beam pumping with doubly-charged OV

Doubly-charged OVs were created at the input of the NLM (see Fig. 1) by a sequence of two identical vortex lenses oriented in the same way (with same helicities) and aligned co-axially. Some representative results for the beam profiles and phases (interference patterns) are shown in the upper and lower row in Fig. 5, respectively. In all newly-generated spectral components we observed doubly-charged OVs. This is in agreement with the expectation that the TC conversion rule follows the rule for converting the photon frequency (energy) in the FWM process. It is also reproduced by our numerical simulations. As seen in the middle frame Fig. 5, near the pump components, at ( $750 \pm 20$ )nm the core of the charge-two OV is well preserved. This can be recognized from the interference fringe that splits into three lines. Since farther-lying spectral components are generated via FWM under non-negligible vortex-ring filamentation, in the component centered at 500nm and in the wavelength range above 900nm the vortex rings are disturbed by filaments. These filaments obviously serve as strong perturbations causing the doubly-charged OVs to decay into singly-charged ones. That is why we observe pairs of slightly offset and still overlapping singly-charged OVs in the left frame in Fig. 5. The OV decay is even stronger pronounced in the range above 900nm (Fig. 5, right frame).

The main results [26] are worth mentioning: If the two pump beams (e.g. at frequencies  $\omega_5$  and  $\omega_6$ ) carry OVs with opposite unit charges, the generated signals at frequencies  $\omega_4$  and  $\omega_7$  carry charge-three vortices of different signs which, eventually, decay into three charge-one vortices with highly overlapping cores. When the input pump beams contain a charge-one OV and a fundamental Gaussian beam, generation of opposite charge-two and charge-one vortices is predicted in the restricted 4-wave model (see Appendix 1). In the complete 10-wave model (see Section 2E for details), due to the cascaded

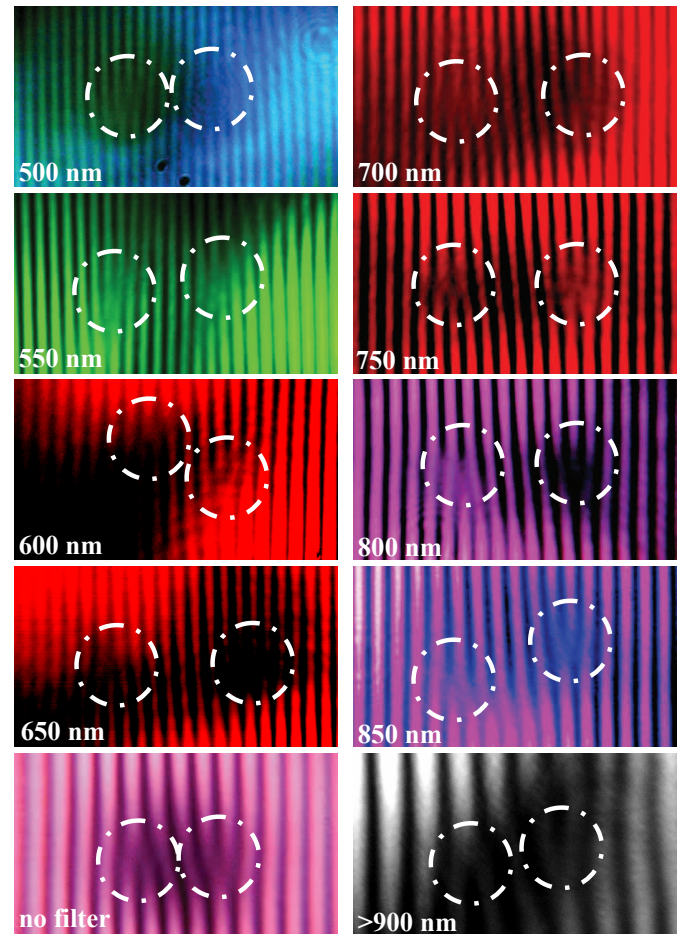


**Fig. 3.** (Color online) Experimental results recorded with the setup shown in Fig. 1. Self-interference of portions of the generated singular white light pre-selected by bandpass filters of 40nm bandwidth, indicating the existence of singly-charged OVs in the pump (near 800nm) and in the newly-generated further-lying spectral components. The respective central wavelengths  $\lambda_c$  of the used filters are denoted. Ar-pressure - 1.3bar.

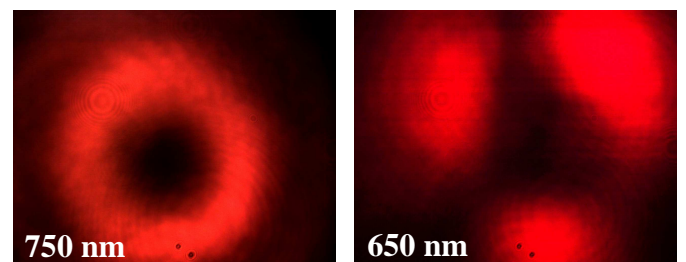


**Fig. 4.** (Color online) Recorded energy-density distribution of the OV beam near the pump (at  $\lambda_c = 750$ nm) and typical energy-density distribution of the newly-generated further-lying spectral components (in the case shown - at  $\lambda_c = 650$ nm). Ar-pressure - 1.3bar.

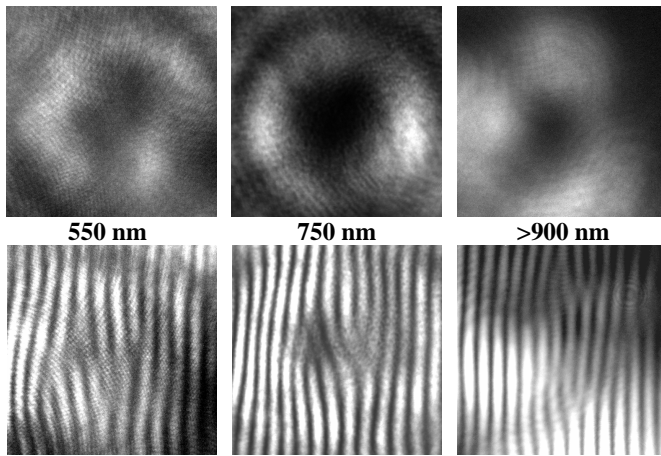


**Fig. 5.** Double-charged pump OVs: Energy-density distributions (upper row) and self-interference (lower row) of some newly generated OVs pre-selected from the white light with bandpass filters. The respective central wavelengths (wavelength-range) are denoted.

nature of the FWM and due to the shifts of the vortex cores, we observed even richer dynamics of the vortices [26]. Generally, the topological charge generated from any two spectral components within the bandwidth of the pump light follows a law analogous to the one for the photon energy in the FWM process. The nonlinear FWM, although not phasematched, is efficient enough to allow for observation of vortices in the spectral satellites over a bandwidth of more than  $\pm 200\text{nm}$  confirming the first measurement of topological charge for a multiply cascaded four-wave mixing process with vortex beams.

### C. Two-beam pumping with singly-charged OVs

Using the input double peaked spectrum (Fig. 2, open circles, and the setup in Fig. 1) we were able to create pump OV beams with equal TCs only (see Sections 2A and 2B). In the two-beam setup (see Fig. 6) the Mach-Zehnder-type interferometer in front of the gas cell provides the possibility to place different combinations of vortex lenses VL in different pump beams. Although in Fig. 7 we present the case of OV stability vs. gas pressure for pumping OVs with  $TC=1$ , we used this scheme in [26] to study the cascaded FWM of OV beams with opposite TCs (+1,-1) and the case of single-charged OV and a Gaussian beam ( $TCs=1$  and 0, respectively). The use of a second, quite different and more complicated setup was important also to prove our experimental findings in a different way.

In order to generate pump vortex beams with a sufficiently large spectral separation, a  $11\text{mJ}$ ,  $36\text{fs}$ ,  $1\text{kHz}$  Ti:Sapphire amplified pulse train is split with a dichroic beam splitter (BS; cut-on wavelength  $800\text{nm}$ ; see Fig. 6). The two beams are sent through additional edge-pass filters (LF and SF) and spiral phase plates VL and are then recombined with a broadband low-dispersion beamsplitter. The two resulting spectral peaks are centred at  $775\text{nm}$  and  $805\text{nm}$ , and will be henceforth denoted as the blue and red pump wavelengths. The spiral phase plates (VLs) are the same 16-step, antireflection-coated fused silica plates optimized for  $790\text{nm}$  that were used in the previous setup. In the reported experiment both VLs imprint a helical phase with  $TC = 1$  onto the beam. After spectral filtering, the average power is  $1.4\text{W}$ , with both overlapping beams having approximately equal intensity. By tilting the filters SF and LF the

width of the gap in the spectrum is chosen to be broad enough to avoid interference of overlapping spectra of the two beams which would disturb the intensity profile. The recombined vortex beams are then focused with a  $f = 2\text{m}$  spherical mirror (FM1, see Fig. 6) into a different  $2.3\text{m}$  long gas cell. The entrance window is the previously used  $3\text{mm}$  thick and Brewster angled fused silica substrate, while the exit window is a  $1\text{mm}$  thick fused silica window oriented perpendicular to the beam propagation direction. The Fresnel reflection from the entrance window is focused onto a CCD camera to monitor the far field beam profile and ensure spatial overlap of the two beams. Temporal overlap is achieved by maximizing the white light emission when the cell is filled with Ar gas. For the actual measurement, the gas cell could be evacuated and nonlinear wave mixing could be observed in the entrance window only. After the gas cell, the beam is recollimated and sent to a second beamsplitter, where it is overlapped with a white-light reference beam. The white-light pulse with no spatial singularity is generated inside a separate gas-filled hollow-core fiber, usually used for few-cycle pulse generation, and is strongly chirped. Therefore, the instantaneous wavelength of the white-light that interferes with the vortex beam is a function of the delay. Because the two pulse trains are extracted from different parts of the amplified femtosecond laser system, we build an additional  $18.6\text{m}$  long delay line to ensure the necessary  $62\text{ns}$  delay for pulse synchronization.

The interference between the vortex beam and the white-light reference beam is observed on another CCD camera in slightly focused geometry. Also the beam profiles of the vortex and reference beams can be recorded. In order to obtain good contrast, the reference beam is attenuated to approximately the same intensity as the vortex beam. As a signature of the vortex helical phase, a dislocation can be seen in the interferogram, which manifests itself as a fork-like splitting of the interference stripes. The interferograms and beam profiles are recorded after different spectral low- and high-pass filters (red and blue LF and SF in the right part of Fig. 6), whose cut-on wavelengths correspond to the gaps between the expected central wavelengths of the satellite spectral components. This method is justified by the fact that the generation efficiency is expected to decrease rapidly with the cascading order of the process. This way, only the dominant part of the spectrum right below or above the filter edge is contributing to the interference pattern. The vortex beam/interference pattern vanishes when either of the two arms in the first Mach-Zehnder interferometer is blocked, as expected for a nonlinear generation mechanism (FWM) of the observed light. For the outermost parts of the spectrum, the intensity is low so that multiple shots (5-10) had to be integrated. Apart from that, the data shown are all single-shot measurements and are highly reproducible from shot to shot ( $< 0.6\%$  peak power fluctuation). This is probably the most proper place to estimate the relative contribution of the nonlinear processes in the cell window and inside the Ar gas. The simplifying assumptions we made are the following:

- i) Most of the nonlinear interaction inside the gas takes place in the filament. This is justified by the short Rayleigh range of  $< 3\text{cm}$  for a  $100\mu\text{m}$  filament diameter.
- ii) The intensity in the filament is assumed to be constant, which is not exactly true.
- iii) The spatial shape of the vortex beam was not taken into account to correct the intensity, but in view of the spectral correction we made, the effect should be minor.

Starting with a Gaussian pulse we ended up with  $2\text{mJ}$  of

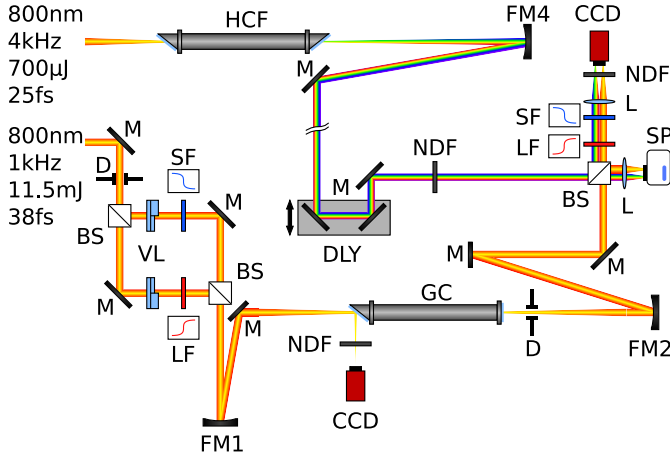


**Fig. 6.** (Color online) Experimental setup for generating white light vortices with separated input pump OV's in both channels. Diagnostics is done with an independent white-light supercontinuum source: M - protected silver-coated mirrors; D - iris diaphragm; VL - vortex lens (16-level spiral phase plate; fused silica); SF - short-pass filter; LF - long pass filter; NDF - neutral-density filters; BS - beam-splitter; FM1 - 2" focusing mirror ( $f = 2m$ ); FM2 - 2" (re)focusing mirror ( $f = 2m$ ); CCD - charge-coupled device camera (Pike F505B, Allied Vision Tech.,  $2452 \times 2054 \text{ pix}$ ,  $3.45 \mu\text{m}$  pixel size); SP - spectrometer (Ocean Optics 2000+). Cell input-up to  $2.2 \text{ mJ}/1 \text{ kHz}$ . Input MZI - ca.  $10 \times 10 \text{ cm}$ . HCF - Ne-filled hollow core fiber for creating white light supercontinuum used later as a reference wave. DLY - adjustable delay line ca.  $18 \text{ m}$  long, ensuring ca.  $62 \text{ ns}$  delay. GC - Ar-filled gas cell  $247 \text{ cm}$  long. FM1-to-cell input -  $127 \text{ cm}$ .

pulse energy (average power of  $2 \text{ W}/1 \text{ kHz}$ ) after all optical elements before the gas cell. This corresponds to a peak power of  $P_{\text{peak}} = 5 \cdot 10^9 \text{ W}$  for the actually measured  $38 \text{ fs}$  pulse duration. The peak intensity on the focusing mirror FM1 (see Fig. 6) we estimate as  $I_{\text{peak}} = 1.2 \cdot 10^9 \text{ W}/\text{cm}^2$  for the wide beam of radius  $1.6 \text{ cm}$ . At the position of the entrance window ( $127 \text{ cm}$  away from FM1) the peak intensity grows to  $I_{\text{peak,window}} = 9.2 \cdot 10^9 \text{ W}/\text{cm}^2$ . To calculate the influence of the nonlinearity, we compare the  $B$ -integral (accumulated nonlinear phase shift) inside the glass with the one inside the gas. We estimate that  $B_{\text{glass}} = (2\pi/\lambda)1.25 \cdot 10^{-8}$ .

For the filament, we first calculate the saturation intensity due to plasma formation [31]

$$I_{\text{sat}} = [2n_{2,\text{Ar}}\rho_{\text{crit}}/(\sigma_K\rho_{\text{neutr}}t_{\text{pulse}})]^{1/(K-1)}, \quad (1)$$

where  $n_{2,\text{Ar}}$  is the nonlinear coefficient of Argon,  $\rho_{\text{crit}}$  is the critical plasma density above which the plasma becomes opaque at  $800 \text{ nm}$ ,  $\sigma_K$  is the  $K$ -photon absorption cross-section,  $\rho_{\text{neutr}}$  is the density of the neutral gas and  $t_{\text{pulse}}$  is the pulse duration. At a pressure of  $1 \text{ bar}$ , with  $n_{2,\text{Ar}} = 1.74 \cdot 10^{-19} \text{ cm}^2/\text{W}$ ,  $\rho_{\text{crit}} = 1.7 \cdot 10^{21} \text{ cm}^{-3}$ ,  $K = 11$ ,  $\sigma_K = 5.04 \cdot 10^{-140} \text{ cm}^{-2}$ , and  $\rho_{\text{neutr}} = 2.69 \cdot 10^{19} \text{ cm}^{-3}$ , we get  $I_{\text{sat}}(p = 1 \text{ bar}) = 4.2 \cdot 10^{13} \text{ W}/\text{cm}^2$ . Due to the  $(K - 1)$ -th-root the scaling of the saturation intensity  $I_{\text{sat}}$  with pressure is relatively weak:  $I_{\text{sat}}(p = 5 \text{ mbar}) = 7.2 \cdot 10^{13} \text{ W}/\text{cm}^2$ , and  $I_{\text{sat}}(p = 2 \text{ bar}) = 3.9 \cdot 10^{13} \text{ W}/\text{cm}^2$ . If we now assume, that most of the nonlinear interaction takes place in a filamentary structure of length  $z = 15 \text{ cm}$ , we can estimate the  $B$ -integral inside the gas according to the relation  $B_{\text{Ar}} = n_{2,\text{Ar}}zI_{\text{sat}}$  and we arrive at  $B_{\text{Ar}}(5 \text{ mbar}) = 9.7 \cdot 10^{-9}$ ,

$B_{\text{Ar}}(1 \text{ bar}) = 1.1 \cdot 10^{-6}$ , and  $B_{\text{Ar}}(2 \text{ bar}) = 2.2 \cdot 10^{-6}$ , respectively. The detailed comparison between the assumed (until now) one-hump pulse spectrum and the (intentionally) used two-hump spectrum indicates a necessary additional correction factor of about  $1.2 - 1.5$  for the pulse intensity inside the glass, and about  $0.7$  for the pulse duration. (We used actually shorter and more intense pulses (compared to Gaussian pulses), of course at the cost of prepulses of lower amplitudes, which we neglect.)

With all necessary corrections, the  $B$ -integrals (with their  $2\pi/\lambda$  multipliers) show that  $B_{\text{glass}} = 0.12$ , whereas  $B_{\text{Ar}}(5 \text{ mbar}) = 0.06$ ,  $B_{\text{Ar}}(1 \text{ bar}) = 7.04$ , and  $B_{\text{Ar}}(2 \text{ bar}) = 13.1$ . We see that in the evacuated cell ( $p = 5 \text{ mbar}$ , the pressure meter accuracy), the influence of the glass is about 2 times that of the gas. Increasing the pressure results in an increase of the nonlinear contribution of the gas by more than 2 orders of magnitude. Qualitatively, this is what we see also in the experiment.

#### D. Vortex stability versus gas pressure

Because a  $1 \text{ kHz}$  pump pulse train was used to create the singular white light and a  $4 \text{ kHz}$  reference white light pulse train came out of the hollow core fiber, we used a B/W CCD camera with an external trigger. All data show in Fig. 7 are single-shot measurements. The first column of frames refer to a moderate Ar pressure of  $p = 1.14 \text{ bar}$ , at which the dominating FWM effect already comes from the gas. In addition to the interferograms for the denoted central wavelengths  $\lambda_c$  of  $\pm 20 \text{ nm}$  of the spectral windows, for the pump components ( $750 \text{ nm}$  and  $800 \text{ nm}$ ) we show also the OV beam energy density distributions. The respective fork-like splittings of the interference lines indicate singly-charged pump OV's. All other interferograms shown in the left column in Fig. 7 (except the somewhat deteriorating picture in the  $900 \text{ nm} - 1000 \text{ nm}$  window) confirm the presence of singly-charged OV's in the newly-generated spectral components. These interference patterns were highly reproducible from shot to shot.

The situation changed when the pressure increased, e.g. to  $p = 1.64 \text{ bar}$ . In the second and third column of frames in Fig. 7 we present more frequently (second column) and less frequently observed (third column) interference structures, along with notation how many singly-charged OV's we could identify. (Frame in the middle column only means that this is a stable and reproducible interference picture). In the  $(550 \pm 20) \text{ nm}$  spectral window, in most cases OV was absent. In relatively rare cases we observed structure, which could be attributed either to  $m$  OV's of alternating unit charges aligned in a line [32], or to a fractional vortex dipole [33]. In the  $(700 \pm 20) \text{ nm}$  window we miss the OV, whereas in the  $850 \text{ nm} - 900 \text{ nm}$  window a pair of oppositely-charged OV's can clearly be identified. Generally, although the instabilities of the OV's near the and inside the filament strongly influence the OV spatial localization at  $p = 1.64 \text{ bar}$ , in most wavelength intervals and in most cases we still identify singly-charged OV's. The observed data can be explained qualitatively in the following way. It is known that the transverse velocity of an OV has a radial and an angular component arising from the transverse phase and intensity gradients, respectively [2, 34]. Once disturbed by the initiated beam filamentation, the OV's probably shift/rotate and overlap with flat portions of the background of the copropagating beam. Therefore, in a certain range of propagation distances the FWM process takes place between beams with unit (say +1) and zero topological charges, which should result in either charge +2 or in charge -1 newly generated signals (see Figs. 1 and 2b [26]), which further split/shift/rotate. Although this

scenario seems to be complicated, it is very likely, because of the relatively poor spatial stability and small transverse extent of the filaments. We do not intend to further speculate on this. What is clear is that for gas pressures, for which the FWFm in the gas already dominates the FWFm in the solid state input window and the vortex beam profile is reproducible, the law for the TC conversion in the different cascades of the FWFm follows the energy conservation law for the same process.

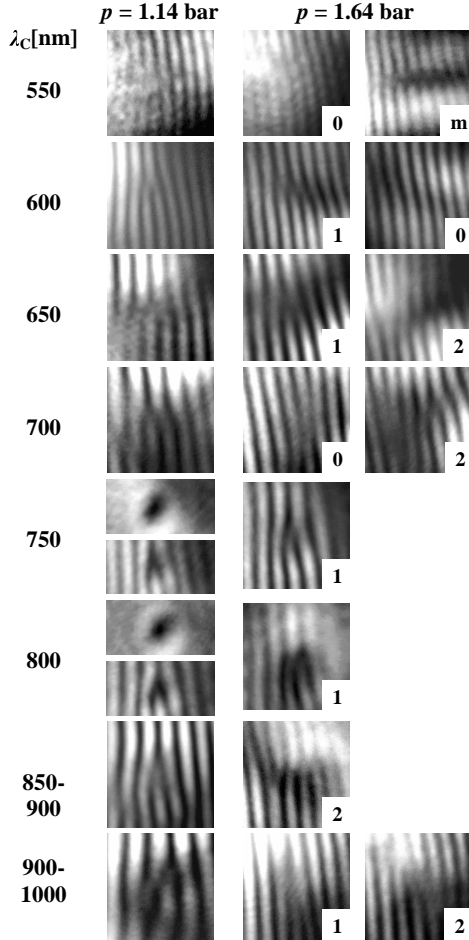


**Fig. 7.** Singly-charged pump OVs. Single-shot interferograms of the white-light vortices taken at two gas pressures and with a separate SC source as a reference wave in the diagnostics (see Fig. 6). The respective central wavelengths of the BP filters are denoted. For the pump OVs at 750nm and 800nm the OV energy-density profiles are shown too. At the high pressure of  $p = 1.64\text{bar}$  the left column shows the most-frequently observed interferograms, the second one (if a picture is shown) - more rarely observed ones. In this case, for clarity, the number of the identified OVs is denoted in each frame. ( $m$ -mixed phase dislocation known also as a fractional OV dipole or  $m$  OVs).

### E. Numerical simulations

In order to numerically simulate the white light generation with (femtosecond) optical vortex beams, we developed an analytical model based on a set of 10 coupled nonlinear partial differential Schrödinger-type equations for the equally-spaced frequency components  $\omega_j$ . It takes into account the two-dimensional beam diffraction, FWFm, as well as self-phase

modulation (SPM) and cross-phase modulation (CPM) effects. We also developed a 28-wave model able to more accurately account for the broadband pump OVs. Since it confirms the main predictions of the 10-wave model, we will present its results only when simulating the output SC spectrum starting from the measured input pump spectrum (see Fig. 9). While the analytical form of the model with ten frequency components is quite cumbersome due to the large number of cross nonlinear terms, an idea of the effects of the involved nonlinear terms can be obtained for the simpler case of 4 involved frequency components (see Appendix 1). The two pump waves in the presented simulations are chosen to have central wavelengths of  $\lambda_c = 780\text{nm}$  and  $800\text{nm}$ . In the complete 10-wave-model, the pump beams have frequencies located in the center of the spectrum,  $\omega_p$  ( $p = 5$  and  $p = 6$ ). When both pump OV beams carry unit topological charges of the same sign, our numerical simulations predict generation of signal beams  $\omega_s$  ( $s = 1..4$  and  $s = 7..10$ ) all carrying OVs of the same charge. This is shown in the examples for  $s = 6$  to 10 in Fig. 8 for the case with no saturation. All data presented in the supplementary material (Figs. 10 and 11 (Appendices 2 and 3)) refer to  $I/I_{\text{sat}} = 2.4 \cdot 10^{-4}$  and account for the 16-step phase profile of the VLs, a certain initial diffraction to the entrance of the gas cell and a certain diffraction from the gas cell to the diagnostics plane, as present in the experiments. While the beam profile is slightly different for each newly-generated spectral component, for singly-charged pump vortices the phases indicate the presence of well defined vortices of charge 1 in all new spectral components (Fig. 10 (Appendix 2)). If the pump OVs are of charge 2 (Fig. 11 (Appendix 3)) all newly generated OVs appear to be doubly-charged.

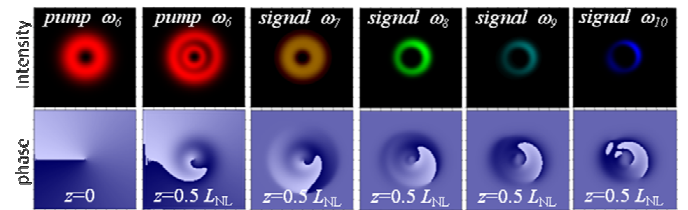


**Fig. 8.** (Color online) Numerical results without saturation of the nonlinearity. Intensity (upper row) and phase (lower row) of one of the pump waves at the entrance ( $z = 0$ ) and at the exit of the nonlinear medium ( $z = 0.5L_{\text{NL}}$ ). Left two columns show the pump beam at the input and at the output of the cell. Right four columns - newly-generated signals due to cascaded FWFm at the output of the cell. For singly-charged pump waves the generated lower-frequency components (not shown here) are symmetric to the higher-frequency ones with respect to the pump waves.

Because our theoretical model is essentially monochromatic (i.e. continuous-wave; see Eqs. 2-4), we run several times the 28-wave numerical simulations, each time with different pump wavelengths. The relative intensities of the selected pump components were chosen accordingly to the measured spectral intensity at the gas cell input as reflections from the Brewster window (Fig. 9, upper plot). The wavelengths/frequencies of the newly-generated components were calculated from the energy conservation law for the FWFm process, thereafter calculating the respective refractive indices and wavenumbers. The spatial integration of each simulated newly-generated spectral component yields one point in the simulated spectral intensity of the generated white light (see Fig. 9, lower plot). As apparent

in the Figure, the numerical simulations reproduce reasonably well the main features of the measured output spectrum, except the (lack of the) peak at  $790\text{nm}$ . While our model neglects the full spatiotemporal dependence in the filamentation process, the pulse SPM and CPM in time and accounts in a simplified way for the influence of the generated plasma in the gas cell, it accurately captures the spectral reshaping of the output beam. However, more sophisticated (3+1)-D models are required to fully capture the inherently complex spatio-temporal dynamics of the process.

Since FWM, SPM and CPM are third-order nonlinear processes, they should be of similar magnitudes. However, while SPM and CPM result in spectral pulse broadening and spatial phase modulation, the process responsible for the transfer of topological charges into the emerging spectral satellites is the FWM. The results shown in Figs. 2-5, along with the simulated output spectrum in Fig. 9, confirm that the generation of ultra-broad vortex beams is due to the cascaded FWM process. The necessary condition to be satisfied is that the spatial effects of the SPM and CPM (beam filamentation and breakup) remain relatively weak in order not to initiate detrimental vortex azimuthal instabilities and loss of transfer of spatial coherence to the newly-generated spectral components. This is especially important (see Fig. 5) for the case of higher-charge vortices, which are much more prone to instabilities.

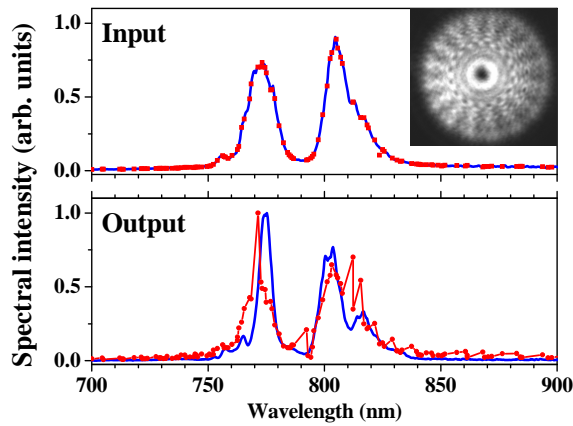


**Fig. 9.** Saturated nonlinearity. (Color online) Numerical results obtained by the 28-wave model of coupled nonlinear equations. Upper graph - input spectrum. Lower graph - output spectrum. Blue curves - experimental data, red dots/curve - input/output data for/from the numerical simulations. Inset - Energy density distribution of a singly-charged OV generated by a vortex lens after free propagation path-length of some  $5m$ . Note the necklace-like oscillations around the vortex core due to the discrete 16 steps in the VL thickness, which are also accounted for in the simulations (see frames at  $z = 2L_{Diff}$  in Fig. 10 (Appendix 2) and Fig. 11 (Appendix 3)).

### 3. CONCLUSION

We have demonstrated broadband cascaded four-wave frequency mixing (FWM) of vortex beams in self-focusing Kerr media (fused silica and Argon). The topological charges of the newly-generated spectral components for pumping light with unit and double topological charges follow a law analogous to the one for the photon energy in the FWM process. Although the FWM is not phasematched, it is efficient enough to allow

for observation of vortices in all spectral satellites over a bandwidth of more than  $\pm 200\text{nm}$ . The results in this work provide strong support of and additional insight into the processes involved in the white light generation by *multiply cascaded* four-wave mixing with femtosecond optical vortex beams.

### 4. APPENDIX 1

In the simplest case of 4 involved frequency components (2 pump waves at frequencies  $\omega_0$  and  $\omega_1$  and 2 signal waves at frequencies  $\omega_{-1}$  and  $\omega_{+2}$ ) [31] the model equations read:

$$i \frac{\partial A_n}{\partial z} + L_D^0 k_n A_n + \frac{k_0}{2k_n} \Delta_{\perp} A_n + \gamma (|A_n|^2 A_n + 2 \sum_{n \neq m} |A_m|^2 A_n + H_n) = 0, \quad (2)$$

( $n, m = -1, 0, +1, +2$ ). Here the terms in the brackets account for SPM and CPM, and

$$\begin{aligned} H_{+2} &= 2A_{-1}^* A_0 A_{+1} \exp(i\Delta k_1 z L_D^0) + A_0^* A_{+1}^2 \exp(i\Delta k_2 z L_D^0), \\ H_{+1} &= 2A_{-1} A_0^* A_{+2} \exp(i\Delta - k_1 z L_D^0) + \\ &\quad 2A_0 A_{+1}^* A_{+2} \exp(-i\Delta k_2 z L_D^0) + A_{-1}^* A_0^2 \exp(i\Delta k_3 z L_D^0), \\ H_0 &= 2A_{-1} A_{+1}^* A_{+2} \exp(i\Delta - k_1 z L_D^0) + \\ &\quad 2A_{-1} A_0^* A_{+1} \exp(-i\Delta k_3 z L_D^0) + A_{+1}^2 A_{+2}^* \exp(i\Delta k_2 z L_D^0), \\ H_{-1} &= 2A_0 A_{+1} A_{+2}^* \exp(i\Delta k_1 z L_D^0) + A_0^2 A_{+1}^* \exp(i\Delta k_3 z L_D^0), \end{aligned} \quad (3)$$

reflect the different possible FWM processes, which depend on the respective phase matching terms

$$\begin{aligned} \Delta k_1 &= k_0 - k_{-1} + k_{+1} - k_{+2}, \\ \Delta k_2 &= 2k_{+1} - k_0 - k_{+2}, \\ \Delta k_3 &= 2k_0 - k_{-1} - k_{+1}. \end{aligned} \quad (4)$$

In the above relations  $k_j$  stands for the wavenumber of the  $j$ -th wave inside the nonlinear medium (Ar gas). Since we assume that initially the two high-intensity pump waves are at frequencies  $\omega_0$  and  $\omega_1$ , it is natural to express the propagation coordinate  $z$  in units of diffraction lengths of one of these waves. We choose normalization to the Rayleigh diffraction length of the optical vortex at frequency  $\omega_0$ , i.e. to  $L_{diff}^0 = k_0 a^2$ , where  $a$  is the radius of the OV beam, being the same for both pump waves. The linear terms in Eq. 2 comprising  $\Delta_{\perp}$  account for the two-dimensional beam diffraction, whereas  $\gamma$  is the saturated Kerr nonlinear coefficient.  $sign(\gamma)$  is positive, reflecting our experimental condition.  $\gamma = \gamma_0 / (1 + I/I_{sat})$  where  $I_{sat} = 4.2 \cdot 10^{13} \text{W/cm}^2$  [31, 36] and  $I = 1 \cdot 10^{10} \text{W/cm}^2$  are chosen to be close to the experimental conditions. In this way we qualitatively account for the influence of both the ionization process and the negative contribution to the medium's refractive index by the generated free electrons in the gas cell. All necessary refractive indices and wave numbers are calculated at these pump wavelengths [37]. The input pump OV beams are described by

$$A = A_0 B(\gamma) \tanh(r/r_0) \exp(il\varphi) \quad (5)$$

where  $A_0$  is the peak field amplitude,  $B(r)$  is the Gaussian beam carrying the optical vortex,  $B(r) = \exp(-r^2/r_{BG}^2)$ ,  $\tanh(r/r_0)$  describes the OV core, and the integer  $l$  is the OV topological charge ( $l = 1$  and  $2$ ; see Fig. 10 (Appendix 2) and Fig. 11 (Appendix 3)). The background beam width  $r_{BG}$  is chosen sufficiently broader than the vortex core  $r_0$ .

## FUNDING INFORMATION

**Funding.** National Science Fund (Bulgaria) - project DFNI-T02/10; DFG (Germany) - in the framework of Forscher-gruppe 532 "Nichtlineare raum-zeitliche Dynamik in dissipativen und diskreten optischen Systemen". DVS acknowledges support from the Government of the Russian Federation (Grant 074-U01) through the ITMO visiting professorship scheme.

## ACKNOWLEDGMENTS

**Acknowledgment.** This work was partially supported by the Australian Research Council. D. N. N. thanks A. Desyatnikov and Y. S. Kivshar for useful discussions. The paper and the participation of D. N. Neshev and A. Dreischuh has been made in the framework of the Erasmus Mundus NANOPHI project, contract number 2013-5659/002-001.

## REFERENCES

- J. F. Nye and M. V. Berry, "Dislocations in wave trains," *Proc. R. Soc. London Ser. A* **336**, 190–191 (1974).
- D. Rozas, C. T. Law, and G. A. Swartzlander, Jr., "Propagation Dynamics of Optical Vortices," *J. Opt. Soc. Am. B* **14**, 3054–3065 (1997).
- A. S. Desyatnikov, Yu. S. Kivshar, and L. Torner, "Optical vortices and vortex solitons," in *Progress in Optics* **47**, Ed. E. Wolf (North-Holland, Amsterdam) 291–391 (2005).
- H. He, M. E. J. Friese, N. R. Heckenberg, and H. Rubinsztein-Dunlop, "Direct observation of transfer of angular momentum to absorptive particles from a laser beam with a phase singularity," *Phys. Rev. Lett.* **75**, 826–829 (1995).
- E. H. Brandt, J. Vanacken, and V. V. Moshchalkov, "Vortices in physics," *Physica C* **369**, 1–9 (2002).
- M. R. Matthews, B. P. Anderson, P. C. Haljan, D. S. Hall, C. E. Wieman, and E. A. Cornell, "Vortices in a Bose-Einstein condensate," *Phys. Rev. Lett.* **83**, 2498–2501 (1999).
- D. G. Grier, "A revolution in optical manipulation," *Nature* **424**, 810–816 (2003).
- G. Foo, D. M. Palacios, and G. A. Swartzlander, "Optical vortex coronagraph," *Opt. Lett.* **30**, 3308–3310 (2005).
- G. Molina-Terriza, J. P. Torres, and L. Torner, "Twisted photons," *Nature Physics* **3**, 305–310 (2007).
- S. Fühapter, A. Jesacher, S. Bernet, and M. Ritsch-Marte, "Spiral interferometry," *Opt. Lett.* **30**, 1953–1955 (2005).
- T. F. Scott, B. A. Kowalski, A. C. Sullivan, C. N. Bowman, and R. R. McLeod, "Two-color single-photon photoinitiation and photoinhibition for subdiffraction photolithography," *Science* **324**, 913–917 (2009).
- A. Picón, A. Benseny, J. Mompert, J. R. Vázquez de Aldana, L. Plaja, G. F. Calvo, and L. Roso, "Transferring orbital and spin angular momentum of light to atoms," *New J. Phys.* **12**, art. 083053 (2010).
- A. Picón, J. Mompert, J. R. Vázquez de Aldana, L. Plaja, G. F. Calvo, and L. Roso, "Photoionization with orbital angular momentum beams," *Opt. Express* **18**, 3660–3671 (2010).
- J. M. Dudley, G. Genty, and S. Coen, "Supercontinuum generation in photonic crystal fiber," *Rev. Mod. Phys.* **78**, 1135–1184 (2006).
- R. Holzwarth, T. Udem, T. W. Hänsch, J. C. Knight, W. J. Wadsworth, and P. St. J. Russell, "Optical frequency synthesizer for precision spectroscopy," *Phys. Rev. Lett.* **85**, 2264–2267 (2000).
- D. M. Brown, K. Shi, Z. Liu, and C. R. Philbrick, "Long-path supercontinuum absorption spectroscopy for measurement of atmospheric constituents," *Opt. Express* **16**, 8457–8471 (2008).
- B. Spokoyny, Ch. J. Koh, and E. Harel, "Stable and high-power few cycle superscontinuum for 2D ultrabroadband electronic spectroscopy," *Opt. Lett.* **40**, 1014–1017 (2015).
- D. J. Jones, S. A. Diddams, J. K. Ranka, A. Stentz, J. L. Hall, and S. T. Cundiff, "Carrier-envelope phase control of femtosecond mode-locked lasers and direct optical frequency synthesis," *Science* **288**, 635–639 (2000).
- O. D. Mücke, R. Ell, A. Winter, J.-W. Kim, J. R. Birge, L. Matos, and F. X. Kärtner, "Self-referenced 200 MHz octave-spanning Ti:Sapphire laser with 50 attosecond carrier-envelope phase jitter," *Opt. Express* **13**, 5163–5169 (2005).
- Y.-W. Tzeng, Y.-Y. Lin, C.-H. Huang, J.-M. Liu, H.-C. Chui, H.-L. Liu, J. M. Stone, J. C. Knight, and S.-W. Chu, "Broadband tunable optical parametric amplification from a single 50 MHz ultrafast fiber laser," *Opt. Express* **17**, 7304–7309 (2009).
- N. Nishizawa, Y. Chen, P. Hsiung, E. P. Ippen, and J. G. Fujimoto, "Real-time, ultrahigh-resolution, optical coherence tomography with an all-fiber, femtosecond fiber laser continuum at 1.5 $\mu$ m," *Opt. Lett.* **29**, 2846–2848 (2004).
- M. C. Stumpf, S. C. Zeller, A. Schlatter, T. Okuno, T. Südmeyer, and U. Keller, "Compact Er:Tb:glass-laser-based supercontinuum source for high-resolution optical coherence tomography," *Opt. Express* **16**, 10572–10579 (2008).
- R. R. Alfano and S. L. Shapiro, "Emission in the region 4000 to 7000Å via four-photon coupling in glass," *Phys. Rev. Lett.* **24**, 584–587 (1970).
- D. N. Neshev, A. Dreischuh, G. Maleshkov, M. Samoc, and Yu. S. Kivshar, "Supercontinuum generation with optical vortices," *Opt. Express* **18**, 18368–18373 (2010).
- G. Maleshkov, D. N. Neshev, E. Petrova, and A. Dreischuh, "Filamentation and supercontinuum generation by singular beams in self-focusing nonlinear media," *J. of Optics* **13**, art. 064015 (2011).
- P. Hansinger, G. Maleshkov, I. L. Garanovich, D. Skryabin, D. N. Neshev, A. Dreischuh, and G. G. Paulus, "Vortex algebra by multiply cascaded four-wave mixing of femtosecond optical beams," *Optics Express* **22**, 11079–11089 (2014).
- A. V. Gorbach and D. V. Skryabin, "Cascaded generation of multiply charged optical vortices and spatiotemporal helical beams in a Raman medium," *Phys. Rev. Lett.* **98**, art. 243601 (2007).
- A. Berzanskis, A. Matijosius, A. Piskarskas, V. Smilgevicus, and A. Stabinis, "Conversion of topological charge of optical vortices in a parametric frequency converter," *Opt. Commun.* **140**, 273–276 (1997).
- Y. Zhang, Z. Nie, Y. Zhao, C. Li, R. Wang, J. Si, and M. Xiao, "Modulated vortex solitons of four-wave mixing," *Optics Express* **18**, 10963–10972 (2010).
- F. Lenzini, S. Residori, F. T. Arecchi, and U. Bortolozzo, "Optical vortex interaction and generation via nonlinear wave mixing," *Phys. Rev. A* **84**, 061801(R) (2011).
- A. Couairon and A. Mysyrowicz, "Femtosecond filamentation in transparent media," *Phys. Rep.* **441**, 47–189 (2007).
- B. Luther-Davies, J. Christou, V. Tikhonenko, and Yu. S. Kivshar, "Optical vortex solitons: experiment versus theory," *J. Opt. Soc. Am. B* **14**, 3045–3053 (1997).
- G. Maleshkov, D. N. Neshev, and A. Dreischuh, "Nonlinear beam steering by fractional vortex dipoles," *Phys. Rev. A* **80**, art. 053828 (2009).
- Yu. S. Kivshar, J. Christou, V. Tikhonenko, B. Luther-Davies, and L. M. Pismen, "Dynamics of optical vortex solitons," *Opt. Commun.* **152**, 198–206 (1998).
- G. Maleshkov, P. Hansinger, I. L. Garanovich, D. Skryabin, D. N. Neshev, A. Dreischuh, and G. G. Paulus, "Degenerate four-wave mixing of optical vortices assisted by self-phase and cross-phase modulation," *Proc. of SPIE* **7747**, art. 77471E (2011).
- A. Braun, G. Korn, X. Liu, D. Du, J. Squier, and G. Mourou, "Self-channelling of high-peak-power femtosecond laser pulses in air," *Opt. Lett.* **20**, 73–75 (1995).
- A. Börzsönyi, Z. Heiner, M. P. Kalashnikov, A. P. Kovács, and K. Osvay, "Dispersion measurement of inert gases and gas mixtures at 800 nm," *Applied Optics* **47**, 4856–4863 (2008).

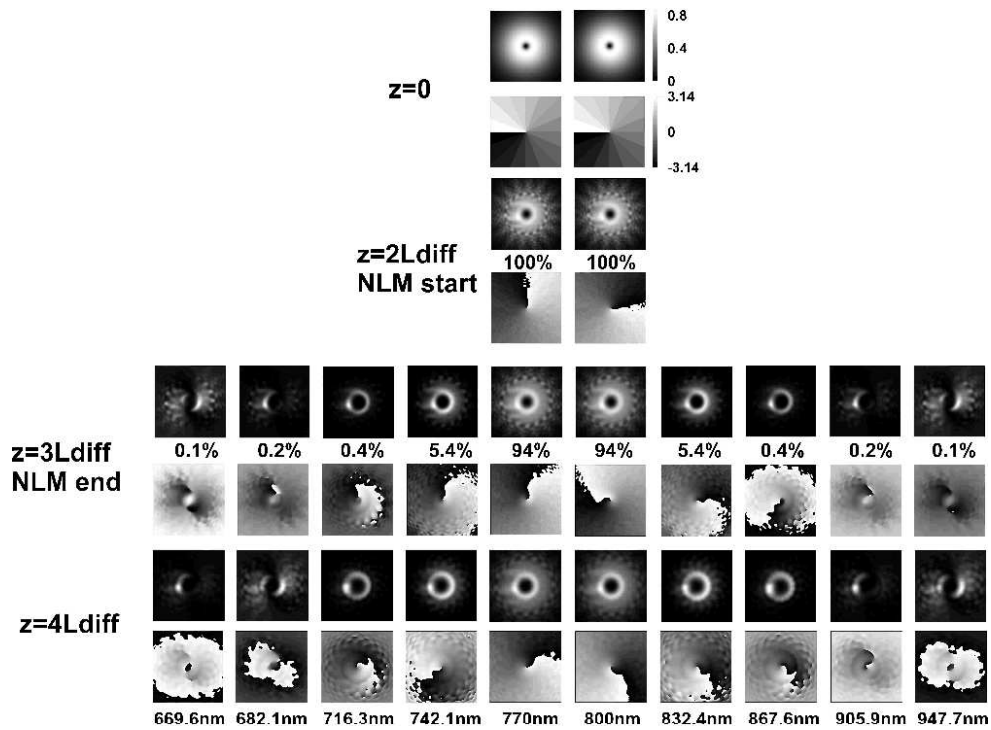


**Fig. 10. Appendix 2:** Saturated nonlinearity. Energy-density (odd rows) and phase distributions (even rows) of the **singly-charged** pump OV just after the spiral phase plates ( $z = 0$ ), at the entrance of the nonlinear medium (NLM) located at  $z = 2L_{diff}$ , at its end ( $z = 3L_{diff}$ ), and at the observation plane located at one diffraction length behind the exit of the NLM. The initial and final diffraction, as well as the 16-level OV input phase distributions are accounted for in order to closely match the experimental conditions.

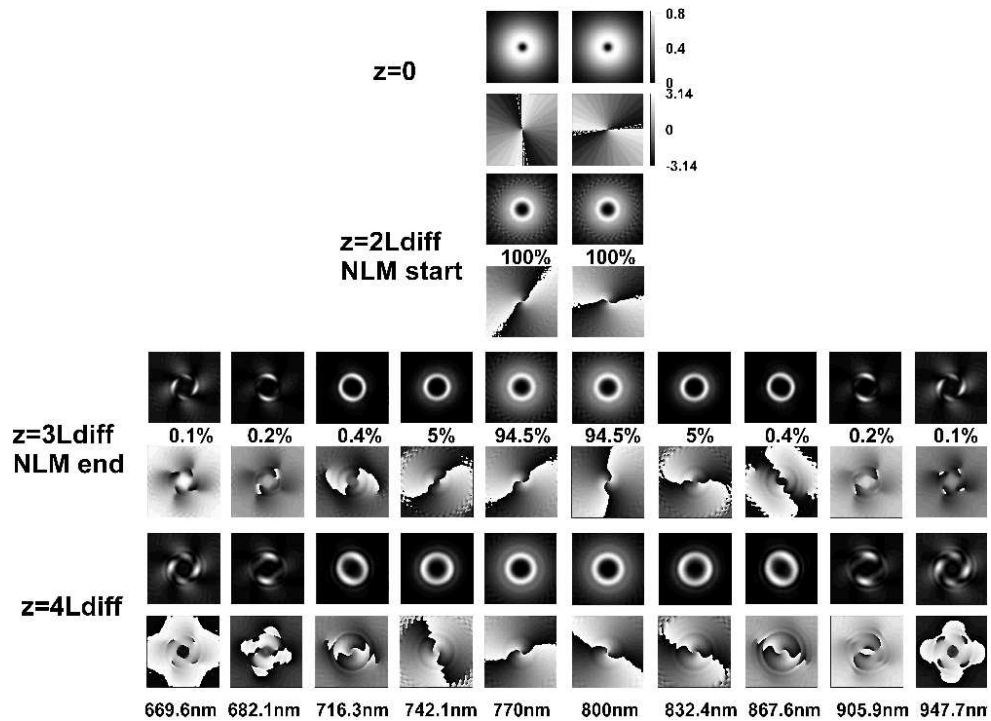


**Fig. 11. Appendix 3:** Saturated nonlinearity. Energy-density (odd rows) and phase distributions (even rows) of the **doubly-charged** pump OV just after the spiral phase plates ( $z = 0$ ), at the entrance of the nonlinear medium (NLM) located at  $z = 2L_{diff}$ , at its end ( $z = 3L_{diff}$ ), and at the observation plane located at one diffraction length behind the exit of the NLM. The initial and final diffraction, as well as the 16-level OV input phase distributions are accounted for in order to closely match the experimental conditions.